NANO · MICRO small
www.small-journal.com

Wearable Textile-Based Co–Zn Alkaline Microbattery with High Energy Density and Excellent Reliability

Yao Wang, Xufeng Hong, Yaqing Guo, Yunlong Zhao, Xiaobin Liao, Xiong Liu, Qi Li, Liang He, and Liqiang Mai**

Wearable in-plane Zn-based microbatteries are considered as promising micropower sources for wearable electronics due to their high capacity, low cost, high safety, and easy integration. However, their applications are severely impeded by inadequate energy density arising from unsatisfactory capacity of cathode and poor cycling stability caused by degradation of electrode materials and Zn dendrite. Additionally, the short-circuit induced safety issue caused by Zn dendrite is still a roadblock for Zn-based microbatteries. Herein, a textile-based Co–Zn microbattery with ultrahigh energy density and excellent cycling stability is demonstrated. Benefiting from the fast electron transport of three-dimensional (3D) porous Ni-coated textile and synergistic effect from the hierarchical $Co(OH)_2$@NiCo layered double hydroxide (LDH) core–shell electrode, the fabricated Co–Zn microbattery with high flexibility delivers superior energy/power densities of 0.17 mWh cm^{-2}/14.4 mW cm^{-2}, outperforming most reported micro energy storage devices. Besides, the trench-type configuration as well as the 3D porous Zn@carbon clothes can avoid the short-circuit-induced safety issues, resulting in excellent cycling stability (71% after 800 cycles). The unique core–shell structure and novel configuration provide a brand-new design strategy for high-performance wearable in-plane microdevices.

1. Introduction

Nowadays, the burgeoning wearable electronics have been devoted to miniaturization, flexibility, stabilization, and easy integration.[1] Thus, the increasing demand for miniaturized electrochemical energy storage devices (MEESDs), especially in-plane MEESDs, have been triggered. In the last decade, microsupercapacitors (MSCs) and micro Li-ion batteries (MLIBs) have been considered as the promising candidates to solve this issue.[2] Unfortunately, the practical applications of MSCs are limited by their inferior energy density while MLIBs are perplexed by the safety issue.[3] Compared with MSCs and MLIBs, the rechargeable alkaline zinc-based microbatteries, especially the Co–Zn alkaline microbattery, are regarded as the competitive alternatives due to their high safety, enhanced capacity, and abundant resource.[4] However, most reported Co–Zn alkaline microbatteries are still suffered from the unsatisfied energy density, poor cycling stability, even short circuit caused by Zn dendrite, obstructing the pervasive applications.[4a,c]

For the conventional in-plane MEESDs, some obstacles are required to overcome. On the one hand, traditional in-plane current collectors based on gold or carbon layer extremely restrict the mass loading of active materials as well as the vertical electronic transmission. On the other hand, most employed technologies for fabricating marco energy storage devices are unhandy to be applied on the micro ones, owing to the compact and fine patterning of MEESDs.[5] Hence, considerable attempts have been focused on constructing 3D microelectrodes through a feasible fabrication process. Currently, textile electrodes have induced a research hotspot due to their high flexibility, artificial 3D porous structure, and easy integration. Especially, the metal modified fabric, constructed by a facile electroless plating process, displayed a comparable conductivity to metal without sacrificing the flexibility.[6] However, conventional micromachining processes such as photolithography and screen printing are impracticable to the fabrication of textile microelectrodes. Encouragingly, the laser method can be a better choice in term of the briefness, speed, and universality.[7] By far, the laser-assisted fabrication of interdigital microelectrodes based on metal modified textile has not been reported yet.

The main obstacles for wide applications of Co–Zn alkaline microbattery are the inferior energy density resulting from the Co-based cathode with low capacity as well as the short circuit caused by Zn dendrite.[8] For Co-based cathode, constructing

Y. Wang, X. F. Hong, X. B. Liao, X. Liu, Prof. Q. Li, Prof. L. He, Prof. L. Q. Mai
State Key Laboratory of Advanced Technology
for Materials Synthesis and Processing
School of Materials Science and Engineering
Wuhan University of Technology
Wuhan, Hubei 430070, China
E-mail: hel@whut.edu.cn; mlq518@whut.edu.cn
Y. Q. Guo
Wuhan National Laboratory for Optoelectronics
Huazhong University of Science and Technology
Wuhan, Hubei 430074, China
Dr. Y. L. Zhao
Advanced Technology Institute
University of Surrey
Guildford, Surrey GU2 7XH, UK
The ORCID identification number(s) for the author(s) of this article can be found under https://doi.org/10.1002/smll.202000293.

DOI: 10.1002/smll.202000293

nanoarchitecture with various morphologies and components is an effective strategy to address this issue. Multifarious Co-based nanoarchitectures such as NiAlCo-layered double hydroxide–CNT hybrid,[9] porous Co_3O_4 nanosheets,[3b] and hierarchical branch-like $Co(CO_3)_{0.5}(OH)_x \cdot 0.11H_2O$@$CoMoO_4$[4b] have been investigated for the cathode materials, and delivered the enhanced capacity as well as the high structural stability. Among these architectures, constructing a hierarchical structure is a valid solution, which can be expected to provide a large surface area, rapid electron/ion transmission, and high structural stability.

For Zn-electrode, Zn dendrite severely limits its electrochemical performance, even punctures the separator resulting in battery shorting.[10] Especially, the safety hazard can be aggravated due to miniaturization of MEESDs. Thus, tremendous efforts have been committed to solving this urgent issue. Current strategies for suppressing Zn dendrite fall into two categories: 1) constructing an antidendrite Zn-electrode by modifying its structure and component; 2) establishing physical isolation between cathode and anode with novel configuration. For instance, Li et al.[4b] reported a 3D carbon clothes–ZnO@carbon skeleton to avoid the formation of Zn dendrite. Higashi et al.[10] designed a backside-plating configuration that handled the internal short circuits. Hence, the search for a feasible approach to fabricate a novel Co–Zn alkaline microbattery with modified anode and configuration is in urgent need.

Herein, a novel textile-based Co–Zn alkaline microbattery is demonstrated for the first time based on 3D flexible microelectrode with trench-type configuration. In detail, a hierarchical $Co(OH)_2$@NiCo-layered double hydroxide@Ni-coated textile (CH@NC–LDH@NT) core–shell architecture as the cathode was fabricated via a typical electroless plating process followed by a two-step strategy, which displayed a considerable areal capacity (0.44 mAh cm^{-2}) and cycling stability (≈93% over 2000 cycles), due to high-speed electronic transmission of 3D network and synergistic effect from the unique core–shell architecture. Besides, short circuit caused by Zn dendrite was validly avoided by a 3D porous Zn@carbon clothes (Zn@CC) anode and well-designed configuration. As a result, the state-of-art Co–Zn alkaline microbattery delivered superb energy/power densities of 0.17 mWh cm^{-2}/14.4 mW cm^{-2} (7.23 mWh cm^{-3}/0.6 W cm^{-3}) and excellent reliability (≈71% after 800 cycles), which exceeded most recently reported MEESDs. Additionally, its high flexibility and skin-touch are highly promising for the wearable electronics.

2. Results and Discussion

The fabrication process of Co–Zn alkaline microbattery is illustrated in **Scheme 1**. First, a piece of pristine textile (4 × 6 cm) was tailored from the lab-gown (Scheme 1b). After electroless plating process, the pristine textile was covered by Ni layers to form the Ni-coated textile (NT) (Scheme 1c). Attractively, the NT exhibits a high electrical conductivity and has a low resistance of about 4.7 Ω (Figure S1, Supporting Information). Then, the hierarchical CH@NC–LDH@NT core–shell electrode was fabricated via a two-step strategy (hydrothermal method and electrodeposition) (Scheme 1d). After that, laser engraving technology was employed to cut the CH@NC–LDH@NT into individual microelectrodes (Scheme 1e). The Zn@CC microanode was fabricated by the similar processes. Finally, the microcathode and microanode were transferred into the corresponding polydimethylsiloxane (PDMS) based

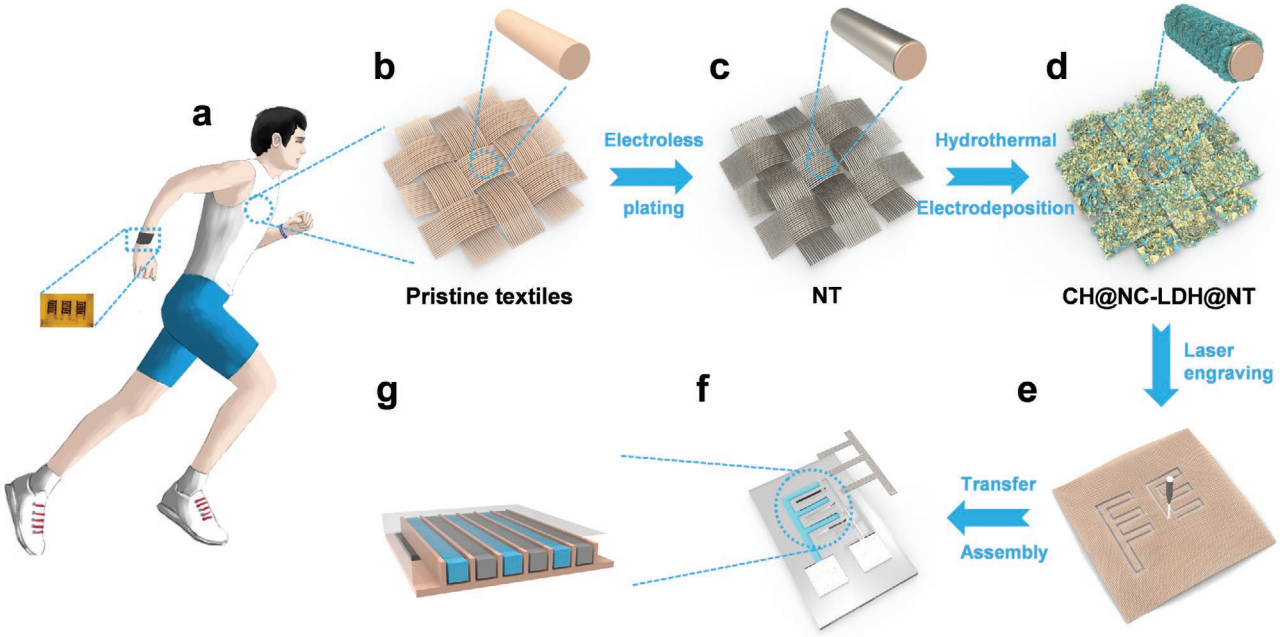

Scheme 1. a) Schematic illustration of the smart textile with the wearable Co–Zn microbattery. The fabrication process of Co–Zn alkaline microbattery: b) a piece of pristine textiles; c) electroless plating of Ni on the textile; d) synthesis of the hierarchical CH@NC–LDH@NT core–shell electrode by hydrothermal method and electrodeposition; e) patterning of microelectrode by laser engraving; f) transferring and assembling the Co–Zn alkaline microbattery; g) the side-view of the fabricated microbattery.

trenches, followed by dropping the gel electrolyte (Scheme 1f). In detail, Scheme 1g shows that the microelectrodes are properly placed in the specific trench filled with gel electrolyte. Additionally, the geometric area of the whole microdevice is only 0.96 cm^2. The microelectrodes have a narrow gap of 0.5 mm and a finger width of 1.5 mm (Figure S2, Supporting Information).

The morphologies and structures of NT, NiCo–LDH@Ni coated textile (NC–LDH@NT), and CH@NC–LDH@NT are shown in **Figure 1**a–c, respectively. The pristine textiles are knitted by the polyester microfiber with a smooth surface and a diameter of 10–15 µm (Figure S3a, Supporting Information). After electroless plating, Ni layers are evenly coated on each polyester fiber with a thickness of 200–300 nm (Figure 1a). By a facile hydrothermal process, NiCo–LDH (NC–LDH) nanosheets are homogeneously coated on the NT with a uniform thickness of 20–30 nm (Figure S3b, Supporting Information). Besides, the wrinkled NC–LDH nanosheets intersect to form a 3D porous interconnected network (Figure 1b). Figure 1c shows the hierarchical CH@NC–LDH@NT core–shell electrode. $Co(OH)_2$ nanoflakes (CH) with smaller size are uniformly distributed on the surface of NC–LDH nanosheets without destroying the original 3D porous network. Moreover, the thickness of shell-liked $Co(OH)_2$ nanoflakes is 10–20 nm.

The crystal structure of hierarchical CH@NC–LDH core–shell electrode was further investigated by transmission electron microscopy (TEM). Especially, the samples for TEM characterization were striped from the CH@NC–LDH coated NT. As shown in the TEM image (Figure 1d), the NC–LDH nanosheets are well assembled with the CH nanoflakes to form the hierarchical core–shell structure. Moreover, the high-resolution TEM (HRTEM) images in Figure 1e display the presence of distinct lattice fringes with *d* spacings of 0.24, 0.28, and 0.46 nm, corresponding to the (101), (100), and (001) planes of $Co(OH)_2$ (JCPDS No. 30-0443) and $Ni(OH)_2$ (JCPDS No. 14-0117), respectively. The annular selected area electron diffraction (SAED) pattern shows the polycrystalline structure of the CH@NC–LDH (Figure 1f). In detail, the diffraction rings are well indexed to (100), (101), (110), and (111) planes of $Ni(OH)_2$ and $Co(OH)_2$. These results are well consistent with the X-ray diffraction (XRD) result of the CH@NC–LDH. The high-angle annular dark-field (HAADF) image in Figure 1g indicates the homogeneous distribution of Ni, Co, and O elements. According to the above results, it is proved that the

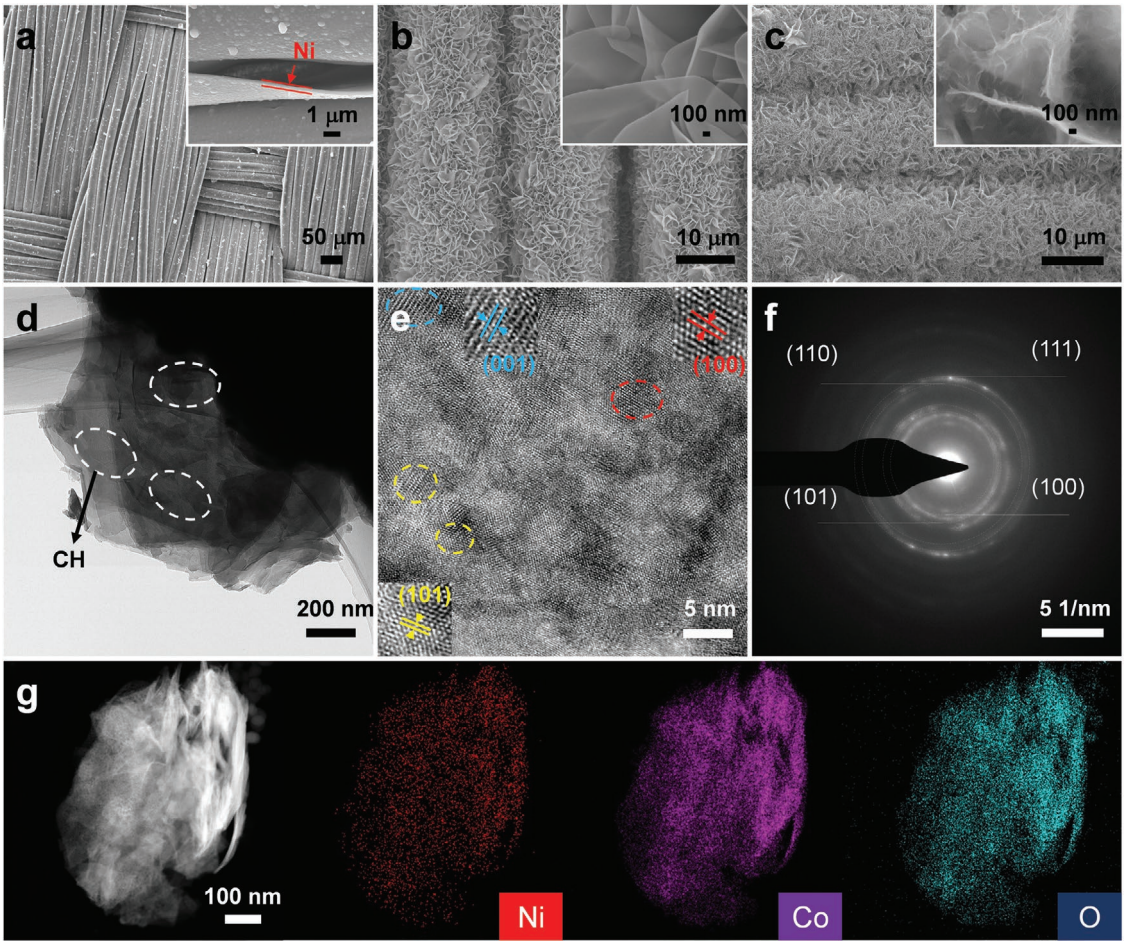

Figure 1. Characterizations of CH@NC–LDH@NT. SEM images of a) NT, b) NC–LDH@NT, and c) CH@NC–LDH@NT. d) TEM images and corresponding e) high-resolution TEM (HRTEM), f) selected area electron diffraction (SAED) images, and g) high-angle annular dark-field (HAADF) and mapping images of CH@NC–LDH.

hierarchical CH@NC–LDH with a core–shell structure was successfully synthesized as expected.

The XRD patterns of NT, NC–LDH@NT, $Co(OH)_2$@Ni-coated textile (CH@NT), and CH@NC–LDH@NT are shown in Figure S4a, Supporting Information. It is obvious that all the XRD patterns have three similar diffraction peaks at 17.6°, 22.8°, and 25.8°, which are attributed to the polymer. A diffraction peak at 44.6° corresponds to the (111) crystal plane of Ni (JCPDS No. 04-0850), which indicates that Ni layers are successfully coated on the polymer textile. The diffraction peaks at 19.3°, 33.4°, 37.8°, 38.5°, 59.7°, and 70.3° correspond respectively to the (001), (100), (101), (002), (003), and (103) crystal planes of $Co(OH)_2$ (JCPDS No. 30-0443) and $Ni(OH)_2$ (JCPDS No. 14-0117). Moreover, Raman spectra of CH@NT, NC−LDH@NT, and CH@NC–LDH@NT are shown in Figure S4b, Supporting Information. The characteristic peaks located at 188, 466, 507, 606, and 670 cm^{-1} correspond to the F_{2g}, E_g, $F_{2g}(2)$, $F_{2g}(1)$, and A_{1g} vibrational modes of $Co(OH)_2$, respectively.[11] Besides, the peak located at 182 cm^{-1} is proper to NiCo–LDH phase.[12] The characteristic peaks located at 475 and 498 cm^{-1} correspond to M–OH and M–O (A_g) stretching modes (M = Ni/Co), respectively.[1c] Another peak located at 650 cm^{-1} indicates that the NC–LDH was synthesized successfully.[13]

X-ray photoelectron spectroscopy (XPS) was applied to study the composition and valence bond of NT, CH@NT, NC–LDH@NT, and CH@NC–LDH@NT (Figure S4c–f; Figure S5, Supporting Information). The survey spectrum of CH@NC–LDH@NT indicates the existence of Ni 2p, Co 2p, O 1s, and C 1s (Figure S4c, Supporting Information). Furthermore, the Ni 2p emission spectrum in Figure S4d, Supporting Information, reveals the presence of two valence states of Ni specie, where two properly divided spin–orbit doublets located at 855.6 and 873.4 eV correspond to Ni $2p_{3/2}$ and Ni $2p_{1/2}$ of Ni^{2+}, while another two peaks at 856.9 and 874.6 eV are ascribed to Ni $2p_{3/2}$ and Ni $2p_{1/2}$ of Ni^{3+}, respectively. The Co 2p spectrum is adequately fitted with two spin–orbit doublets accompanied with shake-up satellites (noted as Sat.) (Figure S4e, Supporting Information). The binding energies at 782.3 and 797.9 eV are indexed to the Co $2p_{3/2}$ and Co $2p_{1/2}$ of Co^{2+} species, while the peaks located at 781.0 and 796.5 eV are attributed to Co $2p_{3/2}$ and Co $2p_{1/2}$ of Co^{3+}, respectively. The O 1s emission spectrum displays two peaks at 531.7 and 531.2 eV, which can be ascribed to the presence of absorbed water and metal hydroxide in the samples (Figure S4f, Supporting Information). The aforementioned results indicate that CH@NC–LDH@NT is composed of the hydroxides of Ni^{2+}, Ni^{3+}, Co^{2+}, and Co^{3+}. On the other hand, the survey spectra of NT, CH@NT, NC–LDH@NT, and CH@NC–LDH@NT are shown in Figure S5a, Supporting Information. As shown in Figure S5b,c, Supporting Information, no signals of Co can be detected in NT as well as inexistence of Ni signals in CH@NT, which are in accordance with high purity of the samples.

The electrochemical performances of NT, CH@NT, NC–LDH@NT, and CH@NC–LDH@NT were explored with three-electrode system, employing a Pt plate as the counter electrode, Hg–HgO as the reference electrode, and 3 M KOH aqueous solution as the electrolyte. Cyclic voltammetry (CV) measurement of as-obtained samples within the working potential window of 0–0.6 V was first carried out at the sweep rate of 5 mV s^{-1}. As shown in **Figure 2**a, NT makes a minor contribution to capacity owing to the insufficient redox reaction during charge–discharge process. For the NC–LDH@NT, two pairs of redox peaks (0.17/0.41 V and 0.26/0.46 V vs Hg/HgO) can be attributed to Ni^{2+}/Ni^{3+} and $Co^{2+}/Co^{3+}/Co^{4+}$ redox couples. The electrochemical reaction equations are displayed as follow.[14]

$$Ni(OH)_2 + OH^- \leftrightarrow NiOOH + e^- + H_2O \quad (1)$$

$$Co(OH)_2 + OH^- \leftrightarrow CoOOH + e^- + H_2O \quad (2)$$

$$CoOOH + OH^- \leftrightarrow CoO_2 + e^- + H_2O \quad (3)$$

However, it is obvious that the redox reaction subjects to regional potential window, while its absence in the low potential area, leading to the restrained capacity. On the other hand, the presence of a pair of redox peaks (0.15/0.06 V vs Hg/HgO) shown in CV curve of CH@NT indicates the transition between $Co(OH)_2$ and CoOOH during the electrochemical processes.[15] In particular, the redox reaction mainly occurs in the low potential area, which can remedy the absence of the capacity. Consequently, CH@NC–LDH@NT integrates the redox reactions of all individual components, which implements a homogeneous distribution of redox area in the whole potential window. Besides, it delivers the highest capacity among the samples due to the synergistic effect from the unique core–shell architecture and 3D porous interconnected network. Figure 2b shows the galvanostatic charge–discharge (GCD) curves of the samples at a current density of 5 mA cm^{-2}. It is obvious that CH@NC–LDH@NT delivers the longest discharge time and the highest discharge plateau among the samples, which are consistent with the results of CV curves. Furthermore, the rate performances of the samples at different current densities are shown in Figure 2c. All samples exhibit good rate performance, while CH@NC–LDH@NT displays the highest capacity. Electrochemical impedance spectroscopy (EIS) measurement was conducted to explore the kinetic process of electron transfer and ion diffusion. A restricted semicircle representing the process of interfacial charge transfer in high-frequency region and a straight line corresponding to the Warburg impedance at low frequencies are observed in Nyquist plots of the samples (Figure 2d). In detail, the EIS of CH@NC–LDH@NT displays the lowest interfacial charge-transfer resistance (R_{ct} = 0.18 Ω) and system resistance (R_s = 1.73 Ω), compared with NT (R_{ct} = 104.2 Ω, R_s = 2.24 Ω), CH@NT (R_{ct} = 0.41 Ω, R_s = 2.23 Ω), and NC–LDH (R_{ct} = 0.77 Ω, R_s = 2.15 Ω). Besides, the CH@NC–LDH@NT exhibits a line with a higher slope than those of other samples, implying the faster electrolyte penetration and ion diffusion than those of other samples. In conclusion, the CH@NC–LDH@NT delivers the superior capacity and excellent rate performance, which is attributed from the following aspects: 1) Ni layers with rough surface provide more active sites and fast electron transfer; 2) NT with 3D porous network provides a larger surface area for assuring high electrolyte-accessible area and shortening the ion diffusion length; 3) synergistic effect from the hierarchical core–shell structure increases the mass loading of active materials, and enhances the electrochemical kinetics.[16]

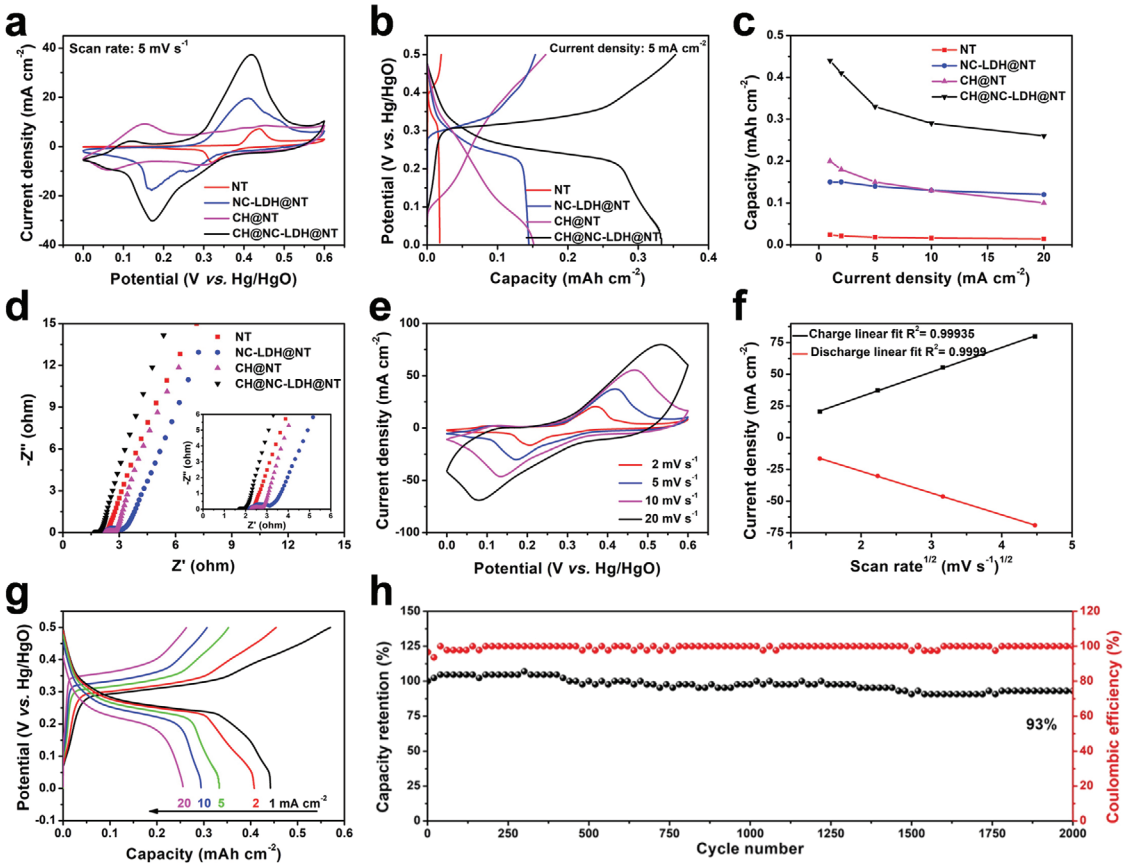

Figure 2. a) Cyclic voltammetry (CV) curves at 5 mV s^{-1}, b) galvanostatic charge–discharge (GCD) curves at 5 mA cm^{-2}, c) rate performance, and d) Nyquist plots of Ni-coated textile (NT), CH@NT, NC–LDH@NT and CH@NC–LDH@NT. e) CV curves, f) linear fitting of i_p versus $v^{1/2}$ curves from the redox peaks in CV curves, g) GCD curves, and h) long-term cycling performance and corresponding Coulombic efficiency of CH@NC–LDH@NT at 20 mA cm^{-2}.

The electrochemical performance of the CH@NC–LDH@NT electrode was further investigated. As shown in CV curves (Figure 2e) at different sweep rates within the range of 2–20 mV s^{-1}, the current density increases with the sweep rate, accompanied with no obvious shape changes but slight shifts of the redox peaks, indicating fast electron transport and good electrochemical reversibility.[14,17] To further investigate the electrochemical kinetic behavior, the relationship between the redox peak currents (i_p) and the scan rates (v) was evaluated, expressed as $i_p = av^b$ (4).[18] In principle, for a battery-type redox reaction constrained by semiinfinite diffusion, i_p is proportional to the $v^{1/2}$, whereas i_p varies with v, corresponding to a capacitive mechanism. As shown in Figure S6, Supporting Information, the b values of the anodic peak and cathodic peak are 0.59 and 0.62, respectively, indicating that the electrochemical process is dominated by diffusion. Besides, Figure 2f shows that both of the i_p of oxidation and reduction can be properly linear fitted with $v^{1/2}$, further indicating that CH@NC–LDH@NT electrodes are battery-type materials.[3a] GCD measurement was carried out to evaluate the capacity and rate performance of the CH@NC–LDH@NT electrode. As shown in Figure 2g, it delivers excellent areal capacities of 0.44, 0.41, 0.33, 0.29, and 0.26 mAh cm^{-2} at current densities of 1, 2, 5, 10, and 20 mA cm^{-2}, respectively. The results manifest that ≈59% of capacity is remained with the increase of current density from 1 to 20 mA cm^{-2}. In addition, Figure 2h displays the long-term cycling performance and corresponding Coulombic efficiency of the CH@NC–LDH@NT electrode at 20 mA cm^{-2}. Remarkably, ≈93% of the areal capacity is retained after 2000 cycles, compared with the initial discharge capacity, indicating an excellent cycling stability. Furthermore, the long lifespan of the CH@NC–LDH@NT electrode was proved by the SEM images of the sample after 2000 cycles. As can be observed in Figure S7, Supporting Information, it is obvious that its morphology and structure are well preserved, ensuring the excellent electrochemical stability.

The Zn dendrite attributed from the inhomogeneous distribution of current, nonuniform flow and restricted mass transport will result in the poor cycle life, even internal shorting.[19] Compared with Zn plates, Zn anodes with a 3D skeleton could provide faster ion diffusion, more reactive sites, and more uniform charge distribution.[3b,4b] Thus, a Zn@CC anode with a 3D porous network was synthesized via a facile electrodeposition process. As shown in Figure S8a, Supporting Information, Zn nanosheets are uniformly coated on each carbon fiber. Besides, the high-magnification SEM image (Figure S8b,c, Supporting Information) shows a 3D porous network constructed by the Zn nanosheets. The synthesized Zn@CC with a 3D porous

network is expected to form a reversible Zn stripping/plating anode. Moreover, the crystal structure of Zn@CC was further characterized by XRD. As displayed in Figure S8d, Supporting Information, all of the diffraction peaks are properly indexed to hexagonal zinc (JCPDS No. 87–0713) except the peak located at 25.7° corresponding to CC.

A wearable Co–Zn alkaline microbattery with a novel trench-type configuration was fabricated via laser engraving method. As shown in Figure S9a, Supporting Information, both of the interdigital CH@NC–LDH@NT cathode and Zn@CC anode are properly placed in PDMS-based microtrenches and fixed by PDMS insulator without any binder. In detail, the horizontal and vertical edges of the microelectrodes were further investigated by optical microscopy (Figure S9b–d, Supporting Information). It is obvious that the PDMS-based insulator takes a role as the wall (noted as "PDMS Wall"), and completely separates the cathode and anode without any structural degradation. What's more, the edges of the electrodes are well-retained without obvious burn mark or crack caused by high energy laser beam. These results indicated that a new-type microbattery was constructed successfully.

For wearable MEESDs, mechanical stability is an essential parameter for practical applications. A series of mechanical tests of the assembled Co–Zn microbattery including lateral bending and vertical bending were conducted. Figure S9e, Supporting Information shows the original Co–Zn microbattery without applied force. Even laterally or vertically bent, the Co–Zn microbattery can still maintain the initial structure as well as the relative positions of the electrodes (Figure S9f,g, Supporting Information). In addition, the Co–Zn microbattery can be directly attached to the skin of human arm, indicating its outstanding capability of integration with other wearable components (Figure S9h, Supporting Information). To further prove the flexibility of the assembled microbattery, the bending tests under different bending angles were conducted with a constant bending radius (R = 10 mm), a device length (L = 30 mm), and diverse bending angles (θ = 0°, 45°, 90° and 180°). As shown in Figure S10a, Supporting Information, the capacity of the assembled Co–Zn microbattery can be retained without distinct decay under various bending angles. Furthermore, the capacity retention after bending with various times was recorded. As shown in Figure S10b, Supporting Information, the Co–Zn alkaline microbattery delivers an excellent performance with the capacity retention of 93.6% after bending tests with 200 times. Owing to the ingenious device design, the assembled Co–Zn alkaline microbattery has high flexibility and wearability.

Electrochemical performances of the assembled Co–Zn alkaline microbattery were further investigated by CV and GCD curves. As shown in **Figure 3**a, the CV curves of the CH@NC–LDH@NT and Zn@CC electrode at 5 mV s^{-1} display a large potential difference of 1.65 V between the redox peaks, indicating a high output voltage of the assembled Co–Zn alkaline microbattery. Moreover, CV curves of the microbattery (Figure 3b) show two pairs of redox peaks without obvious shape change at different scan rates, indicating sufficient redox reaction and good electrochemical reversibility of the microbattery. The overall electrochemical reaction is described as following.

$$\mathrm{Zn} + \mathrm{CoOOH} + \mathrm{NiOOH} + 2\mathrm{KOH} + 2\mathrm{H_2O} \leftrightarrow \mathrm{K_2[Zn(OH)_4]} + \mathrm{Ni(OH)_2} + \mathrm{Co(OH)_2} \quad (5)$$

As shown in Figure 3c, attributed from the rapid electron and ion transfer of the microbattery, all the GCD curves display characteristic charge and discharge plateaus at ≈1.68 and ≈1.64 V with a small voltage hysteresis of ≈0.1 V. In addition,

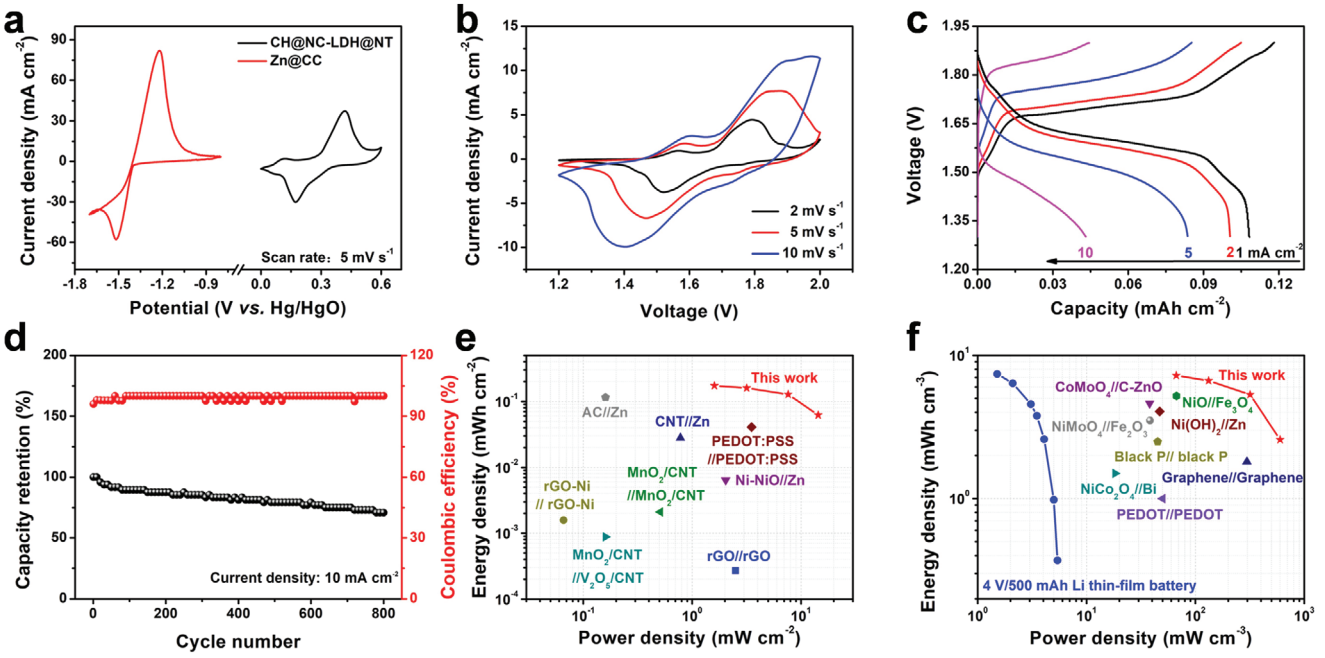

Figure 3. Electrochemical performances of Co–Zn microbattery. a) Cyclic voltammetry (CV) curves of CH@NC–LDH@NT and Zn@CC at 5 mV s^{-1}. b) CV curves, c) galvanostatic charge–discharge (GCD) curves, d) long-term cycling stability, and e,f) Ragone plots of Co–Zn microbattery.

Figure S11a, Supporting Information, shows that the Co–Zn microbattery delivers remarkable areal capacities of 108.3, 100.6, 83.6, and 43.1 μAh cm^{-2} at various current densities of 1, 2, 5, and 10 mA cm^{-2}, respectively. Prominently, the charge–discharge time of the assembled microbattery at 10 mA cm^{-2} is only about 32 s, which is lower than that of the conventional Ni–Zn battery.[20] EIS is composed of a restricted semicircle (R_s = 15.7 Ω, R_{ct} = 0.42 Ω) and a straight line with the high slope, suggesting the rapid electron transfer and high ion diffusion coefficient of the microbattery (Figure S11b, Supporting Information). These results are consistent with the corresponding fitting equivalent circuit.

The long-term cycling stability of the Co–Zn alkaline battery was studied at 10 mA cm^{-2}. As observed in Figure 3d, it delivers an excellent cycling performance with capacity retention of 71% over 800 cycles along with nearly 100% Coulombic efficiency. Furthermore, the morphology and structure of the CH@NC–LDH@NT cathode and Zn@CC anode after long-term cycling are shown in Figure S12, Supporting Information. It is obvious that both of CH@NC–LDH@NT core–shell structure and Zn nanosheets were mainly reserved after cycling, which results in excellent cycling stability.

Furthermore, the current density simulation analysis was conducted to investigate the antidendrite function of trench-type configuration. Additionally, the formation of Zn dendrite can be induced by the inhomogeneous distribution of current. The dendrites grow larger when there is the higher local current density.[19] Figure S13a, Supporting Information, shows a conventional in-plane Co–Zn microbattery with a Zn plate as the anode. During charge–discharge process, the electric field distribution is mainly concentrated in the gap area (Figure S14a, Supporting Information). Owing to the higher current density of the gap area than that of top area (Figure S13b, Supporting Information), Zn dendrites are mainly formed on the surface of the gap area and grow laterally, resulting in short circuit (Figure S13c, Supporting Information). Whereas, for the trench-type configuration (Figure S13d, Supporting Information), the electric field distribution is regulated by the PDMS Wall (Figure S14b, Supporting Information). As shown in the current density profile of trench-type configuration (Figure S13e, Supporting Information), the current density of the top area is higher than that of the gap area. Accordingly, Zn dendrites are mainly formed on the top surface of Zn plate and grow toward the inclined top area, which can not lead to short circuit (Figure S13f, Supporting Information). Therefore, the novel trench-type configuration can provide a secondary protection, while the aforementioned 3D porous Zn@CC electrode plays the role as the first protection.

For the in-plane MEESDs, the areal energy/power densities are more valuable since the gravimetric values are unconsidered.[1a] Noticeably, the Co–Zn alkaline microbattery delivers superb areal energy density of 0.17 mWh cm^{-2} (Figure 3e and Table S1, Supporting Information), which exceeds those of most reported energy storage devices including CNT//Zn (0.028 mWh cm^{-2}),[21] Ni–NiO//Zn (0.0066 mWh cm^{-2}),[8] and MnO_2/CNT//V_2O_5/CNT (0.00088 mWh cm^{-2}).[22] In addition, it displays the maximum areal power density of 14.4 mW cm^{-2}, much higher than that of the symmetric MSC, such as rGO (2.51 mW cm^{-2}),[23] PEDOT:PSS (3.52 mW cm^{-2}),[24] and MnO_2–CNT (0.51 mW cm^{-2}).[25] On the other hand, the intrinsic performance of the electrode material can be further assessed by volume energy/power densities.[26] Thus, the volume energy/power densities were further evaluated (Figure 3f and Table S2, Supporting Information). The Co–Zn alkaline microbattery exhibits excellent volume energy/power densities of 7.23 mWh cm^{-3}/0.60 W cm^{-3}, higher than those of the recently reported MSC, alkaline microbattery (Ni–Zn,[27] Co–Zn,[4b] and Ni–Fe microbattery[28]), and even the Li thin-film battery. More interestingly, three words of "WUT" composed of 42 green light-emitting diodes (LEDs) can be lighted by three serially connected microbatteries (Figure S15, Supporting Information). The excellent performances of the Co–Zn alkaline microbattery can be attributed to the following reasons: 1) the 3D porous NT provides high-speed path way for electronic transmission. Besides, high flexibility and wearability of NT are remained. 2) The hierarchical CH@NC–LDH@NT core–shell electrode provides the porous structure, which synergistically improves the efficiency of ion transport as well as the structure stability. 3) Double protection is induced to avoid short circuit. One is the 3D porous Zn@CC anode which accelerates homogeneous distribution of current, the other is the well-designed configuration providing a barrier to interdict the electrode contact and induces the oriented growth of Zn dendrite.

3. Conclusion

In summary, a facile and feasible approach is proposed and adopted to fabricate a high-performance in-plane Co–Zn alkaline microbattery with a novel device design. The key to the facile fabrication process is the microfabrication of flexible microelectrode. The hierarchical CH@NC–LDH@NT core–shell electrode was fabricated via the electroless plating combined with the hydrothermal method and electrodeposition. The Co–Zn microbattery delivers a high performance, owing to the 3D high-speed electronic transmission network and synergistic effect from the hierarchical core–shell structure. Furthermore, by employing the laser engraving method and transfer molding process, the integrated microelectrode and flexible patterned reservoir are fabricated, respectively. The rational trench-type configuration can effectively hinder the short circuit caused by electrode contact and Zn dentrite. The assembled Co–Zn alkaline microbattery delivers superb energy/power densities (0.17 mWh cm^{-2}/14.4 mW cm^{-2}) and excellent cycling stability (capacity retention of 71% over 800 cycles). We demonstrate an ingenious fabrication process for microbattery as well as a rational device design, which establishes a new strategy for development of micropower sources in flexible and portable electronics.

4. Experimental Section

Fabrication of the Ni-Textile: A piece of the discarded lab-gown textile was completely cleaned by acetone, ethanol, and deionized (DI) water in an ultrasonic bath. Subsequently, Ni layers were deposited on the textile by a typical electroless plating process. First, the clean textile was roughed by the solution of 15 g L^{-1} $KMnO_4$ and 40 mL L^{-1} 38% HCl at 40 °C for 5 min, and then the obtained textile was washed

with 12 g L^{-1} $H_2C_2O_4$ solution at 30 °C for 3 min to remove the residual MnO_4^-. Subsequently, the roughed textile was sensitized by the solution of 10 g L^{-1} $SnCl_2$ and 40 mL L^{-1} 38% HCl for 20 min, and then the obtained textile was activated by the solution of 0.5 g L^{-1} $PdCl_2$ and 20 mL L^{-1} 38% HCl for 20 min. Finally, the obtained textile was immersed in the mixed solution of 0.1 mol L^{-1} $NiSO_4$, 20 g L^{-1} $Na_3C_6H_5O_7$, and 30 g L^{-1} NaH_2PO_2 at 80 °C for 20 min, resulting in Ni layers deposited on the textile. Ni-Textile was washed by ethanol and DI water for several times and dried in vacuum oven.

Fabrication of Interdigital Microelectrode: Briefly, CO_2 Universal Laser Cutter System (model: Universal VLS 2.30) was employed to fabricate the interdigital microelectrode by direct laser engraving. Nevertheless, the parameters of laser power and cutting speed were set dissimilarly owing to the difference between the applied materials of positive electrode and negative electrode. For the fabrication of interdigital CH@NC–LDH@NT microelectrode, the laser power was adjusted to 20 W, and the speed was set to 30%. Distinctly, for the fabrication of Zn@CC microelectrode, the laser power decreased to 15 W, and the speed decreased to 2%, owing to the flammable carbon clothes. As the process finished, both of the microelectrodes were successfully fabricated.

Fabrication of Interdigital CH@NC–LDH@NT Microelectrode: The NC–LDH nanosheets array was successfully synthesized on the Ni-textile via a facile hydrothermal process. 2 mmol $Ni(NO_3)_2{\cdot}6H_2O$, 4 mmol $Co(NO_3)_2{\cdot}6H_2O$, and 8.8 mmol HMTA were dissolved in 40 mL DI water and 20 mL ethanol to form a transparent pink solution. Subsequently, a piece of Ni-textile (3 × 5 cm) was immersed in the mixed solution with ultrasonic treatment for 10 min. The obtained mixture was then transferred to teflon-lined autoclave and kept at 90 °C for 8 h. After cooling down to room temperature, the sample was washed by ethanol and DI water for several times and dried in vacuum oven. Consequently, the mass loading of the obtained NC–LDH is about 1.02 mg cm^{-2}. In addition, a typical constant potential electrodeposition was carried out to synthesize the CH@NT–LDH core–shell structure, accompanied with a Pt plate as the counter electrode, a saturated calomel electrode (SCE) as the reference electrode, and the NC–LDH@NT as the work electrode. Accompanied with the three-electrode system immersed in 0.05 M $Co(NO_3)_2$ aqueous electrolyte, a constant potential of –1.0 V was applied for 10 min, resulting in the synthesis of CH@NC–LDH@NT. The samples were washed by ethanol and DI water for several times and dried in vacuum oven. Consequently, the mass loading of CH@NC–LDH is about 1.8 mg cm^{-2}. Finally, the interdigital CH@NC–LDH@NT microelectrode was successfully fabricated following the direct laser engraving process.

Fabrication of Interdigital Zn@CC Microelectrode: A piece of carbon clothes (2 × 2 cm) was completely washed with acetone, ethanol, and DI water in an ultrasonic bath, and dried in vacuum oven. Consequently, carbon clothes based interdigital microelectrode was fabricated in advance by the direct laser engraving process owing to Zn@CC burning during the laser cutting process. A typical electrodeposition was performed in the mentioned three-electrode system to deposit Zn nanoflakes on the carbon clothes based interdigital microelectrode. Briefly, the carbon clothes based interdigital microelectrode used as the work electrode was immersed in the mixed solution of 124 g L^{-1} $ZnSO_4{\cdot}7H_2O$ and 75 g L^{-1} Na_2SO_4. A constant current density of 20 mA cm^{-2} was applied for 30 min, resulting in the synthesis of Zn@CC microelectrode. The samples were washed with ethanol and DI water for several times and dried in vacuum oven.

Fabrication of Interdigital Co–Zn Microbattery: A PDMS-based interdigital microelectrode groove was successfully fabricated by a facile transfer molding process. Briefly, an SU8-50 photoresist-based seal was fabricated by a typical photolithography process. Subsequently, PDMS elastomer and curing agent (mass ratio of 10:1) were homogeneously stirred followed by eliminating air bubbles under vacuum for 10 min. Then, the mixture was evenly smeared on the SU8-50 photoresist-based seal and transferred to a heating stage at 100 °C for 20 min followed by peeling the PDMS-based interdigital microelectrode groove off. On the other hand, the interdigital microelectrodes were soaked in the aqueous–gel electrolyte and respectively transferred into the grooves followed by dropping the electrolyte, and the interdigital alkaline microbattery was assembled.

Numerical Simulation: COMSOL multiphysics (COMSOL Inc.) was applied for simulating the electric field distribution in the trench-type configuration. First, a two-dimensional model was set up, including the electrolyte, electrodes, and insulated walls. All dimensions of electrodes are consistent with the sizes of the actual devices. Besides, the gap between the insulated wall and electrode is 50 μm. The heights of the electrode, insulated wall, and electrolyte are 3, 3.5, and 4 mm, respectively. The input voltage on the electrodes is 1.6 V. Then, Nernst–Planck equation was used to evaluate the current density and electric field distribution of the electrolyte. The given ionic conductivity of the KOH electrolyte is 0.6 S cm^{-1}.

Materials Characterization: The morphology and microstructure were characterized by SEM (JEOL JSM-7100F) and TEM (JEM-2100F/Titan G2 60–300). XRD patterns were determined by a D8 Discover X-ray diffractometer with Cu K_α radiation (λ = 1.5418 Å). Raman spectroscopy measurement was carried out by a Renishaw INVIA micro-Raman spectroscopy system. XPS analysis was performed by a VG MultiLab 2000 instrument.

Electrochemical Characterization: The electrochemical performances were measured by a CHI 760E Electrochemical Workstation (CH Instruments, China) with two-electrode and three-electrode systems at room temperature. For the single electrode electrochemical measurement, the three-electrode system was carried out in 3 M KOH aqueous electrolyte, accompanied with a Pt plate as the counter electrode, a Hg–HgO electrode as the reference electrode, and the cathode/anode sample as the work electrode. Otherwise, the two-electrode system was conducted in 3 M KOH aqueous–gel electrolyte with CH@NC–LDH@NT as cathode and Zn@CC–Zn plate as anode for the alkaline microbattery electrochemical measurement. Particularly, the KOH gel electrolyte (3 M KOH–PVA) was prepared by the following method: first, the mixture of 3 g PVA dissolved in 30 mL DI water was stirred at 85 °C for 3 h to form a transparent solution, followed by the solution (20 mL) of 8.415 g KOH with saturated ZnO instilled drop by drop and stirred homogeneously to acquire the gel electrolyte. The specific capacity (C) of electrode was calculated based on the following formula: $C = It/A$, where I is the discharge current (mA), t is the discharge time (h), and A is the area (cm^2) of the electrode. Besides, the energy density (E) and the power density (P) of the alkaline battery were calculated based on the following formula: $E = I\int U(t)dt/B$ and $P = E/t$, where I is the discharge current (mA), $U(t)$ is the discharge voltage, t is the discharge time, and B is the area (cm^2) or volume (cm^3) of the electrode. EIS measurement was carried out by employing a AC voltage of 5 mV amplitude within the frequency scope of 100 kHz to 0.01 Hz at open circuit potential.

Supporting Information

Supporting Information is available from the Wiley Online Library or from the author.

Acknowledgements

This work was supported by the National Key Research and Development Program of China (2016YFA0202603), the National Natural Science Foundation of China (51832004, 51521001, 51425204), the Programme of Introducing Talents of Discipline to Universities (B17034), and the Yellow Crane Talent (Science & Technology) Program of Wuhan City.

Conflict of Interest

The authors declare no conflict of interest.

Keywords

Co–Zn microbatteries layered double hydroxide, trench-type configuration, wearable batteries

Received: January 15, 2020
Revised: February 22, 2020
Published online:

[1] a) C. Lethien, J. Le Bideau, T. Brousse, *Energy Environ. Sci.* **2019**, *12*, 96; b) N. A. Kyeremateng, T. Brousse, D. Pech, *Nat. Nanotechnol.* **2017**, *12*, 7; c) W. Liu, M. S. Song, B. Kong, Y. Cui, *Adv. Mater.* **2017**, *29*, 1603436; d) H. Li, Z. Tang, Z. Liu, C. Zhi, *Joule* **2019**, *3*, 613.

[2] a) J. I. Hur, L. C. Smith, B. Dunn, *Joule* **2018**, *2*, 1187; b) D. Qi, Y. Liu, Z. Liu, L. Zhang, X. Chen, *Adv. Mater.* **2017**, *29*, 1602802.

[3] a) P. Simon, Y. Gogotsi, B. Dunn, *Science* **2014**, *343*, 1210; b) X. Wang, F. Wang, L. Wang, M. Li, Y. Wang, B. Chen, Y. Zhu, L. Fu, L. Zha, L. Zhang, Y. Wu, W. Huang, *Adv. Mater.* **2016**, *28*, 4904; c) L. Xu, S. Tang, Y. Cheng, K. Wang, J. Liang, C. Liu, Y. C. Cao, F. Wei, L. Mai, *Joule* **2018**, *2*, 1991.

[4] a) J. F. Parker, C. N. Chervin, I. R. Pala, M. Machler, M. F. Burz, J. W. Long, D. R. Rolison, *Science* **2017**, *356*, 415; b) M. Li, J. Meng, Q. Li, M. Huang, X. Liu, K. A. Owusu, Z. Liu, L. Mai, *Adv. Funct. Mater.* **2018**, *28*, 1802016; c) Q. Yang, G. Liang, Y. Guo, Z. Liu, B. Yan, D. Wang, Z. Huang, X. Li, J. Fan, C. Zhi, *Adv. Mater.* **2019**, *31*, 1903778; d) Z. Hao, L. Xu, Q. Liu, W. Yang, X. Liao, J. Meng, X. Hong, L. He, L. Mai, *Adv. Funct. Mater.* **2019**, *29*, 1808470.

[5] J. Q. Xie, Y. Q. Ji, J. H. Kang, J. L. Sheng, D. S. Mao, X. Z. Fu, R. Sun, C. P. Wong, *Energy Environ. Sci.* **2019**, *12*, 194.

[6] D. Wang, Y. Zhang, X. Lu, Z. Ma, C. Xie, Z. Zheng, *Chem. Soc. Rev.* **2018**, *47*, 4611.

[7] Q. Jiang, N. Kurra, C. Xia, H. N. Alshareef, *Adv. Energy Mater.* **2017**, *7*, 1601257.

[8] a) Y. Zeng, Y. Meng, Z. Lai, X. Zhang, M. Yu, P. Fang, M. Wu, Y. Tong, X. Lu, *Adv. Mater.* **2017**, *29*, 1702698; b) Y. Huang, Z. Li, Z. Pei, Z. Liu, H. Li, M. Zhu, J. Fan, Q. Dai, M. Zhang, L. Dai, C. Zhi, *Adv. Energy Mater.* **2018**, *8*, 1802288.

[9] M. Gong, Y. Li, H. Zhang, B. Zhang, W. Zhou, J. Feng, H. Wang, Y. Liang, Z. Fan, J. Liu, H. Dai, *Energy Environ. Sci.* **2014**, *7*, 2025.

[10] S. Higashi, S. W. Lee, J. S. Lee, K. Takechi, Y. Cui, *Nat. Commun.* **2016**, *7*, 11801.

[11] J. Yang, H. Liu, W. N. Martens, R. L. Frost, *J. Phys. Chem. C* **2010**, *114*, 923.

[12] C. Zhang, J. Zhao, L. Zhou, Z. Li, M. Shao, M. Wei, *J. Mater. Chem. A* **2016**, *4*, 11516.

[13] K. Qin, L. Wang, S. Wen, L. Diao, P. Liu, J. Li, L. Ma, C. Shi, C. Zhong, W. Hu, E. Liu, N. Zhao, *J. Mater. Chem. A* **2018**, *6*, 8109.

[14] G. Nagaraju, S. Chandra Sekhar, L. Krishna Bharat, J. S. Yu, *ACS Nano* **2017**, *11*, 10860.

[15] T. Deng, W. Zhang, O. Arcelus, J. G. Kim, J. Carrasco, S. J. Yoo, W. Zheng, J. Wang, H. Tian, H. Zhang, X. Cui, T. Rojo, *Nat. Commun.* **2017**, *8*, 15194.

[16] T. Zhao, G. Zhang, F. Zhou, S. Zhang, C. Deng, *Small* **2018**, *14*, 1802320.

[17] J. Zhao, Z. Li, X. Yuan, Z. Yang, M. Zhang, A. Meng, Q. Li, *Adv. Energy Mater.* **2018**, *8*, 1702787.

[18] a) M. R. Lukatskaya, B. Dunn, Y. Gogotsi, *Nat. Commun.* **2016**, *7*, 12647; b) H. S. Kim, J. B. Cook, H. Lin, J. S. Ko, S. H. Tolbert, V. Ozolins, B. Dunn, *Nat. Mater.* **2017**, *16*, 454; c) Z. Liu, Q. Yang, D. Wang, G. Liang, Y. Zhu, F. Mo, Z. Huang, X. Li, L. Ma, T. Tang, Z. Lu, C. Zhi, *Adv. Energy Mater.* **2019**, *9*, 1902473.

[19] V. Yufit, F. Tariq, D. S. Eastwood, M. Biton, B. Wu, P. D. Lee, N. P. Brandon, *Joule* **2019**, *3*, 485.

[20] X. Pu, L. Li, M. Liu, C. Jiang, C. Du, Z. Zhao, W. Hu, Z. L. Wang, *Adv. Mater.* **2016**, *28*, 98.

[21] G. Sun, H. Yang, G. Zhang, J. Gao, X. Jin, Y. Zhao, L. Jiang, L. Qu, *Energy Environ. Sci.* **2018**, *11*, 3367.

[22] J. Yun, Y. Lim, H. Lee, G. Lee, H. Park, S. Y. Hong, S. W. Jin, Y. H. Lee, S. S. Lee, J. S. Ha, *Adv. Funct. Mater.* **2017**, *27*, 1700135.

[23] X. Pu, M. Liu, L. Li, S. Han, X. Li, C. Jiang, C. Du, J. Luo, W. Hu, Z. L. Wang, *Adv. Energy Mater.* **2016**, *6*, 1601254.

[24] Z. Wang, J. Cheng, Q. Guan, H. Huang, Y. Li, J. Zhou, W. Ni, B. Wang, S. He, H. Peng, *Nano Energy* **2018**, *45*, 210.

[25] Z. Lv, Y. Luo, Y. Tang, J. Wei, Z. Zhu, X. Zhou, W. Li, Y. Zeng, W. Zhang, Y. Zhang, D. Qi, S. Pan, X. J. Loh, X. Chen, *Adv. Mater.* **2018**, *30*, 1704531.

[26] M. Beidaghi, Y. Gogotsi, *Energy Environ. Sci.* **2014**, *7*, 867.

[27] a) J. Liu, C. Guan, C. Zhou, Z. Fan, Q. Ke, G. Zhang, C. Liu, J. Wang, *Adv. Mater.* **2016**, *28*, 8732; b) C. Xu, J. Liao, C. Yang, R. Wang, D. Wu, P. Zou, Z. Lin, B. Li, F. Kang, C. P. Wong, *Nano Energy* **2016**, *30*, 900.

[28] a) C. Guan, W. Zhao, Y. Hu, Q. Ke, X. Li, H. Zhang, J. Wang, *Adv. Energy Mater.* **2016**, *6*, 1601034; b) K. A. Owusu, L. Qu, J. Li, Z. Wang, K. Zhao, C. Yang, K. M. Hercule, C. Lin, C. Shi, Q. Wei, L. Zhou, L. Mai, *Nat. Commun.* **2017**, *8*, 14264.